Journal of Physics D:
Applied Physics

PAPER • **OPEN ACCESS**

Secondary electron emission for reticulated carbon foam surfaces using direct measurements and spectroscopic analysis

To cite this article: Angelica Ottaviano *et al* 2025 *J. Phys. D: Appl. Phys.* **58** 465204

OPEN ACCESS
IOP Publishing
Journal of Physics D: Applied Physics
J. Phys. D: Appl. Phys. **58** (2025) 465204 (13pp)
https://doi.org/10.1088/1361-6463/ae18e1

Secondary electron emission for reticulated carbon foam surfaces using direct measurements and spectroscopic analysis

Angelica Ottaviano[1,5,*], Gary Wan[1], Yevgeny Raitses[2], Evan T Ostrowski[3], Shota Abe[2], Bruce E Koel[3] and Richard E Wirz[1,4]

[1] Mechanical and Aerospace Engineering, University of California, Los Angeles, CA, United States of America
[2] Princeton Plasma Physics Laboratory, Princeton, NJ, United States of America
[3] Chemical and Biological Engineering, Princeton University, Princeton, NJ, United States of America
[4] Mechanical, Industrial, and Manufacturing Engineering, Oregon State University, Corvallis, OR, United States of America

E-mail: angelica.ottaviano@g.ucla.edu

Received 12 May 2025, revised 21 October 2025
Accepted for publication 29 October 2025
Published 14 November 2025

Abstract

This study investigates secondary electron emission (SEE) characteristics of reticulated foams using direct measurements and analytical modeling. Total SEE was quantified, revealing suppression of up to 44% in carbon foam structures compared to planar graphite surfaces. An optimal geometric configuration was identified and supported by analytical models. SEE angular dependence experiments showed diverse behaviors: fiber-like behavior and directional dependence for pore and ligaments on the mm scale, with fuzz-like characteristics when the foam features are between 10–100 μm. Electron energy analyzer measurements showed that carbon foams preferentially suppress inelastic backscattered electrons (BSEs) more so than true secondary electrons (SEs). The analysis indicated a larger fraction of low-energy SE generation in foams compared to flat surfaces due to increased emission from curved fiber ligaments and tertiary SEs from high-energy BSEs. These findings have implications for design and optimization of materials with tailored electron emission properties for applications like plasma-facing components, spacecraft materials, and accelerator surfaces.

Keywords: secondary electron, emission, carbon, foam, micro-engineered, Auger

[5] Current affiliation: Thea Energy, Inc.
[*] Author to whom any correspondence should be addressed.

1. Introduction

Secondary electron emission (SEE) occurs when an energetic primary particle, such as an electron, impacts a material surface [1, 2]. SEE influences plasma–surface interactions, for example by modifying sheath properties and associated heat fluxes to walls [3], as well as by contributing to anomalous transport and plasma discharge instabilities [4].

In many charged particle applications, SEE is an adverse effect. It causes multipactor breakdown in radio-frequency (RF) components [5, 6], contributes to plasma cooling in electric thrusters [7], and may lead to anomalous charging of spacecraft surfaces [8–10]. SEE may also cause performance degradation in particle accelerators by initiating electron cloud build-up that drives beam instabilities [11, 12]. Experimental studies have quantified SEE from fusion plasma-facing materials such as lithium and lithium compounds [13] and nanostructured tungsten fuzz [14], as well as from dielectric materials relevant to Hall thruster channel walls, including boron nitride [15]. Numerical models that explicitly include SEE have also demonstrated its impact on sheath formation [16], electron velocity distributions in confined plasmas [17], and avalanche processes in liquids [18]. In geospace contexts, SEE affects spacecraft–plasma interactions and wave excitation [19, 20].

Recent studies have addressed several aspects of SEE, including the difficulty of obtaining reliable low-energy yield data [21], emission from spacecraft insulators [22], its influence on plasma probe design [23], and measurements from complex propulsion-relevant surfaces [24]. SEE has also been applied as a diagnostic, for example in inferring surface electrostatic potential [25, 26], and it forms the operating principle of electron multipliers and photomultiplier tubes [27–29].

Given its wide-ranging impact, accurately characterizing a material's intrinsic SEE properties is required. To this end, the measurements reported in this work are conducted in a simplified setup under high-vacuum and ultrahigh vacuum conditions. This controlled environment isolates the effects of material composition and surface geometry from external variables like surface contamination and gas-phase electron scattering. Such fundamental experiments provide a baseline for predicting material performance in complex systems where plasma interactions and external fields can influence electron behavior and introduce errors in diagnostic measurements [30, 31].

Computational studies have examined SEE reduction from various structured surfaces, such as velvets [32], micro-porous arrays designed to suppress electron clouds in accelerator devices [33], and foams or fuzz [34]. Furthermore, Monte Carlo ray-tracing methods have been adapted to simulate SEE from arbitrarily complex geometries, with reticulated foams used as a key demonstration case [35]. Experimental work has shown that plasma-infused foams suppress sputtering through geometric trapping [36], while SEE reduction has been reported for other reticulated surfaces [37, 38]. A motivation for the study of foams is that compared to planar surfaces, they retain volumetric complexity under erosion [39, 40], and may also exhibit self-healing through re-deposition. Foam morphology is defined by ligament size, pore dimension, and overall thickness [38, 41]. This study examines open-cell reticulated carbon foams with ligament and pore sizes from tens of μm to several mm.

Previous studies of SEE from foams have included scanning electron microscopy (SEM)-based yield estimation [42] and direct current measurements [14, 37], while related computational work has modeled electron transport in complex morphologies [43]. Studies of other engineered materials, such as velvets [42] and tungsten fuzz [14] also emphasize the role of surface geometry in modifying SEE.

Secondary electrons (SEs) are generally divided into 'true' SEs and backscattered electrons (BSEs). True or low-energy SEs originate from within the target material and are emitted due to the interaction with an energetic primary electron and by overcoming the material work function. True SEs are generated within the first 1–50 nm of the surface [44] and are defined to have energies below 50 eV [45, 46]. BSEs are reflected primary electrons that are either inelastically BSEs (iBSEs), thus losing some of their energy through the material surface during collisions with core electrons, or elastically BSEs (eBSEs), producing reflected electrons with the same energy as the incident electrons. Other inelastic scattering products include plasmons, phonons, and polaron excitations. Auger electrons may also be emitted following energetic electron bombardment of a surface, and the detection of these electrons forms the basis for Auger electron spectroscopy (AES) [47, 48]. Auger emission is a three-electron non-radiative transition following ionization generated by electron interaction with the material, producing electrons that are element-specific with energies dictated by the electron transitions involved.

The total SEE yield γ_{tot} is defined as the sum of true (γ_{SE}) and backscattered (γ_{BSE}) SE yields:

$$\gamma_{\mathrm{tot}} = \gamma_{\mathrm{SE}} + \gamma_{\mathrm{BSE}}. \tag{1}$$

The BSE yield which can be expressed as the sum of iBSE yield γ_{iBSE} and eBSE yield γ_{eBSE}:

$$\gamma_{\mathrm{BSE}} = \gamma_{\mathrm{iBSE}} + \gamma_{\mathrm{eBSE}}. \tag{2}$$

This work aims to characterize the total SEE yield from reticulated carbon foams with a direct measurement setup [49–52], as well as to analyze the SEE energy spectrum using a cylindrical mirror analyzer (CMA) setup typically used for AES. In previous work, Patino *et al* [53] used 4-grid optics typically applied for low energy electron diffraction (LEED) with a scanning bias to acquire SE energy distribution functions (SEEDFs), showing that for planar graphite with incident primary energies above 100 eV, the total contribution of true SEs was ≈85% of the total SEE yield, while ≈12%–14% was from iBSEs or rediffused electrons, and the remaining 1%–3% was from eBSEs. These results were in good agreement with empirical models and previous measurements [47, 54]. In the work described herein, a setup for directly measuring SEE current was used to find γ_{tot} from reticulated carbon surfaces.

To further examine the mechanisms by which SEs are generated and trapped in reticulated materials, a novel application of an AES setup was used to directly measure the SE energy spectrum from planar and non-planar, reticulated carbon surfaces. The Auger spectroscopy setup consists of a CMA with a coaxial electron gun, an electron multiplier detector, and an electron analyzer power supply. With this data, it was possible to study the relative contribution of true SEs, iBSEs and eBSEs to the total SEE yield by integrating SEEDFs acquired with the CMA.

2. Experimental setup and target samples

2.1. Reticulated carbon foam samples

Four reticulated carbon foams manufactured by ERG Aerospace Duocel [41, 55] were analyzed in these experiments. Similar foams were used in recent work [38] where the SEE yield was estimated using SEM. Figure 1 shows optical images of the foams measured in these experiments. Reticulated foams are geometrically characterized by their average pore diameter, D, and ligament diameter, d. A common linear metric for foam materials is pores per inch (PPI), which is defined as:

$$\mathrm{PPI} = \frac{1\ \mathrm{inch}}{D+d} \tag{3}$$

as well as the foam characteristic aspect ratio, A_R, defined as:

$$A_\mathrm{R} = D/d. \tag{4}$$

The transparency, T, of a reticulated foam is defined in the direction parallel to an incident particle beam as the ratio of exposed backplate area to the total projected surface area of the foam. A simple exponential equation describes the percent transparency of a foam given a thickness, and a ligament and pore diameter and was derived and detailed in ref [38, 56]. T was calculated for each of the foams used in the direct SEE yield experiments and was found to vary from ≈0 transparency for a 100 PPI foam to 20% transparency for a 5 PPI foam. Because of this range in transparencies, it is important to carefully consider any backplate contribution to the SEE yield. To this end, a planar graphite disk was mounted in combination with the carbon foams.

Table 1 summarizes the geometric properties of the foam samples. It is important to note that often the indicated manufacturing PPI of a foam is not the actual measured PPI of the foam received. This is critical when comparing SEE model results to SEE experimental measurements where the input parameters are geometric variables such as A_R, d, and D. Several images of each foam used in the SEE yield direct measurement experiments were taken by an optical microscope and scaled using Motic Imaging Software. The foam properties reported in table 1 were generated from averaging 25 ligament and pore diameters observed for each foam sample.

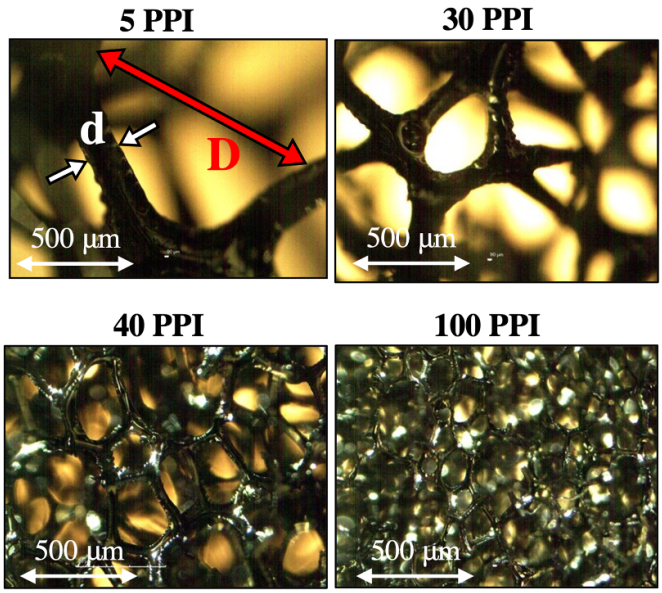

Figure 1. Selected optical microscope images of foams used for SEE yield measurements. PPI values were calculated by averaging 25 measurements of pore and ligament diameters from each carbon foam.

2.2. Direct SEE measurements

Direct measurements of the total SEE yield of the reticulated carbon foams were taken using a dedicated experimental setup at the Princeton Plasma Physics Laboratory Nanolab and has been described in Ref [49]. The setup consists of a high vacuum chamber that has a base pressure of 1–5 × 10^{-7} Torr and an ELG-2 Kimball Physics electron gun which produces electrons with a range of energies between 5–1000 eV. The maximum beam current to the target was kept at $< 1\ \mu$A. In order to shield out stray electric fields, an electrically isolated aluminum collector plate was attached to the electron gun and installed over the target sample. A schematic of the setup with a foam target is shown in figure 2.

Because the samples have pore dimensions ranging from 45 μm–1.4 mm (table 1), it was important to ascertain that the electron beam is large enough to cover more than one pore in a single measurement. The requirement for the electron beam diameter was thus determined to be:

$$\phi_\mathrm{e} > D \tag{5}$$

where ϕ_e is the electron beam diameter at the sample surface. A graphite Faraday cup with an entrance opening diameter of 0.5 mm was first used to characterize and center the electron beam before measuring the reticulated carbon samples. The Faraday cup was mounted onto a ceramic base that is attached to an aluminum arm linear stage. The stage can move the Faraday cup perpendicular to the electron beam. The electron beam profile was measured by positively biasing the inner pillar of the Faraday cup and recording currents with a picoammeter. The electron beam profile and shape depends on the primary energy (PE) and can be modified with the focus voltage settings. Guidance from data reported in the Kimball

Table 1. Geometric properties of the reticulated carbon foams used in direct SEE yield measurements[a].

Indicated PPI	Measured PPI	D [μm]	d [μm]	$A_R = D/d$	T[%]
10	5	1370 ± 150	320 ± 58	4.3	20
30	30	1060 ± 122	200 ± 44	5.3	10
60	40	590 ± 80	70 ± 20	8.4	5
100	100	210 ± 32	45 ± 12	4.7	0.1

[a] Each foam has the same thickness of 6.35 mm. The indicated PPI is that given by the manufacturer, while the measured PPI is calculated from measuring scaled microscope images of the foams. The measured foam PPIs have a spread of ± 2 PPI.

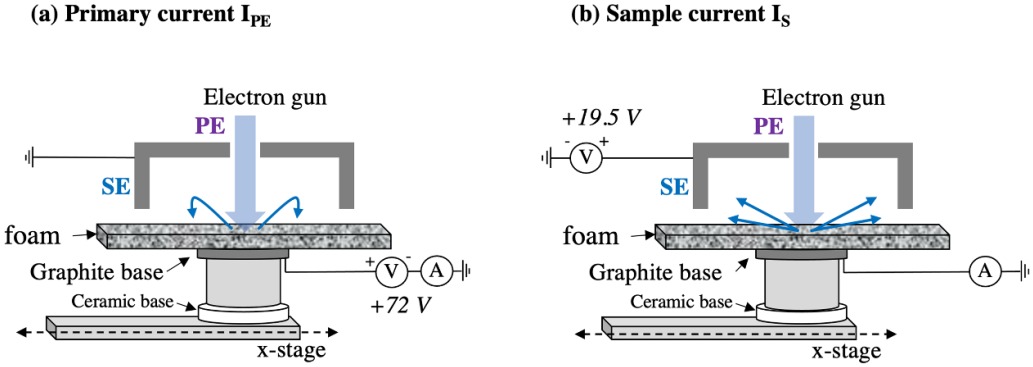

Figure 2. Setup and electrical connections for measuring (a) the primary current of the electron beam, and (b) the sample current. The x-stage can also be rotated around its central axis for incident electron beam angle studies.

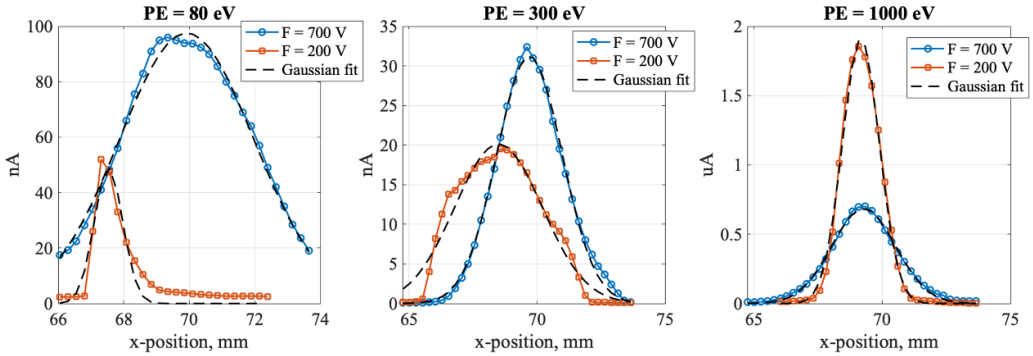

Figure 3. Primary incident electron current measured using an electrically grounded Faraday cup with a 0.5 mm diameter aperture versus position for three different electron gun incident energies of 80 eV, 300 eV, and 1000 eV and two focus voltage settings for each of $F =$ 700 V (blue) and $F = 200$ V (red). The black dashed lines are Gaussian fits for each beam profile, where the standard deviation was found by measuring where the beam radius is equal to $1/e^2$ of its peak value.

ELG-2 manual was used to select two focus voltage settings to characterize the electron beam for low (80 eV), middle-range (300 eV) and high (1000 eV) beam energies. These two focus voltages were $F = 700$ V and 200 V. Figure 3 shows the profiles with a Gaussian fit for each setting used. Based on these measurements, it was determined that the $F = 700$ V setting was suitable for all primary beam energies with a beam diameter ranging from $\phi_e = 2$–6 mm, which satisfies the electron beam diameter requirement. The beam center was also determined for each setting by finding the center of the Gaussian profile fits by measuring its standard deviation.

For SEE yield measurements, a polished graphite plate was placed behind the carbon foams, as shown in figure 2. This was done so that in the case of low PPI foams with nonzero transparency to the primary electron beam, SEs are generated from only carbon surfaces. The foams are each 6 cm $\times$ 3 cm $\times$ 0.64 cm while the graphite disk has a 2.54 cm diameter and 0.1 cm thickness. The foams were bound to the graphite disk with a 22 AWG copper wire, and were then placed onto a cylindrical aluminum sample holder. The aluminum holder was in turn mounted to a ceramic base so that the sample could be electrically isolated and biased with respect to the electron gun. For the primary current measurement, I_{PE}, the sample was biased to + 72 V with respect to ground to suppress and collect SEs as well as measure the incident current provided by the electron gun, and the collector was connected to ground. For the sample current measurement I_S, the sample was connected to ground while the collector was biased to + 19.5 V. These two biases were experimentally determined by performing voltage sweeps on the sample

and collector to respectively find the onset of saturation for the primary beam current and for the SE current. With this configuration, the sample current is $I_S = I_{PE} - I_{tot}$, where I_{tot} is the total SEE current comprised of SEs and BSEs which is directed to the collector. In addition, tertiary electrons from the chamber walls were prevented from being collected by the sample. The total SEE yield is then determined by:

$$\gamma_{tot} = \frac{I_{tot}}{I_{PE}} = \frac{I_{PE} - I_S}{I_{PE}} = 1 - \frac{I_S}{I_{PE}}. \quad (6)$$

Each reticulated carbon sample was measured at five adjacent locations on the surface so that an average spread in the SEE yield could be calculated. For measuring the incidence electron beam angle dependence of the SEE yield, the sample stage was tilted around its central axis by -20° to$+30^\circ$. In the case of a nonzero transparency foam, the SEE yield was measured with and without the graphite backplate by moving the linear stage so that the electron beam can penetrate the foam in a region where there is no backplate. In figure 2, this is where the foam hangs off the edge of the graphite plate past the reach of the aluminum arm mount. During measurements for a foam with no backplate, a fraction of the electron beam proportional to the transparency of the foam is dumped to the chamber ground and not collected by the picoammeter.

2.3. Electron spectroscopy using a CMA

For a complete analysis of SEE, a dedicated ultrahigh vacuum chamber for surface science studies at the Surface Science and Technology Laboratory at PPPL was used for electron spectroscopy. In these studies, the chamber had a base pressure of 1×10^{-8} Torr. A double pass CMA (Perkin-Elmer PHI 15-255) used in that chamber for AES and x-ray photoelectron spectroscopy was used for these experiments discussed herein to analyze the SEs from flat graphite and a reticulated carbon structure. Operation of the CMA utilized a PHI 20-805 electron analyzer control unit, PHI 20-075 electron multiplier supply, and a RBD 147 interface unit (RBD Instruments) for computer interfacing using the AugerScan III software. The CMA consists of two concentric cylindrical electrodes that can have different applied voltages to collect different electron energies at the detector. A coaxial electron gun is installed at the centerline of the CMA to produce a primary electron beam. The number of SEs, both true and backscattered, as a function of their kinetic energies were obtained by operating the CMA in the AES mode. For these experiments, the CMA was operated at a fixed energy resolution of 0.6% of the electron kinetic energies. The acceptance angle of the CMA for electrons emitted from the target material is around a $42.5^\circ \pm 6^\circ$ angle from the target surface normal around a complete 360° azimuthal angle. The electron multiplier voltage of 1650 V was used for all measurements.

One-hundred PPI carbon foam with dimensions $5 \times 5 \times 3$ mm was placed above an equivalently sized flat graphite sample on a translatable sample mounting block, and the chamber setup is shown in figure 4. The graphite and carbon

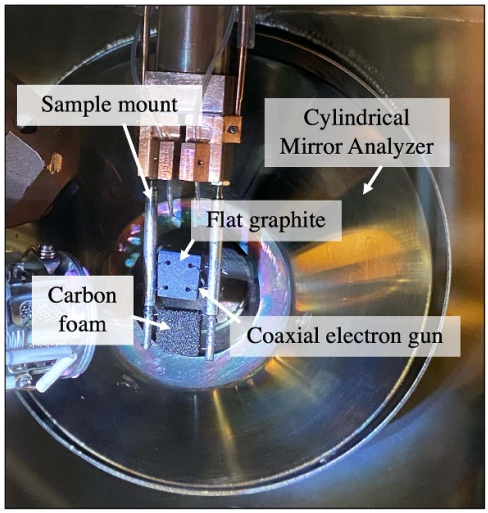

Figure 4. CMA with coaxial electron gun facing two samples. The sample mount can move vertically with a motorized stage so that the graphite and foam can be positioned at the CMA and electron gun focus for consecutive alternating measurements.

foams were vertically mounted with tantalum wires that were spot-welded onto two larger tantalum rods. The vertical shaft is controlled by a motorized stage, so that either the graphite or the foam can be aligned to the electron gun and CMA system for measurement. Electrically, the sample was connected to a picoammeter in series to ground so that the collected current from the electron gun, I_{PE}, could be monitored and recorded.

Each measurement was taken for three graphite and foam locations and averaged. Example semilog spectra from the flat graphite at incident primary beam energies of 100, 200, 300, 400 and 500 eV are shown in figure 5. The resolution of each spectrum was 0.5 eV, and the dwell time for each data point was 80 ms. The increasing background signal is due to the constant retarding ratio mode of the electron analyzer, which results in an increasing window with increasing kinetic energy (KE). Thus, the electron analyzer signal was removed by dividing each spectrum by the electron KE. Three datasets were taken at three different locations for each PE (100, 200, 300, 400, 500, 800, and 1000 eV) on the graphite and foam samples and averaged to analyze the electron spectroscopy of carbon foams. Figure 5 shows curves for select PE energies of 100, 200, 300, 400, and 500 eV to demonstrate the data handling. The small peaks observed at kinetic energies lower than each of the elastically backscattered energy peaks are due to specific energy losses by the BSEs due to plasmon interactions and excitations [57].

Spectra for the flat graphite sample and a foam sample are shown in figure 6 for a PE of 300 eV. The measured currents to the sample are typically between 100–500 nA for primary energies between 100 and 1000 eV. This type of energy spectrum analysis allows for the comparison of true secondary and backscattered SE yield between a flat graphite and a foam structure. Calculations of true SE, iBSE and eBSE are performed directly from these spectra by integrating sections of the curves. The three SE populations are indicated

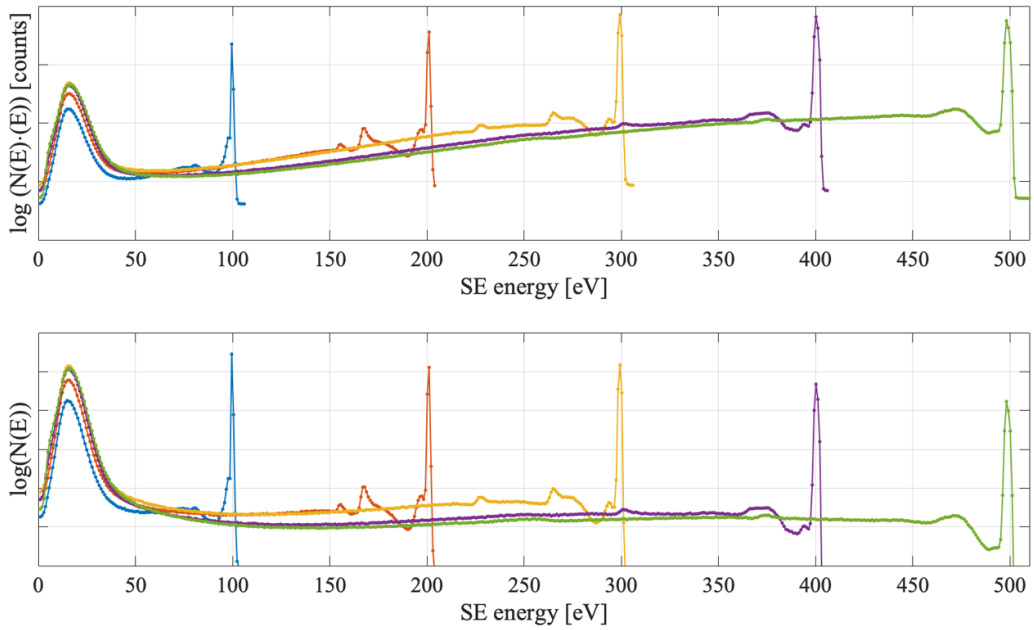

Figure 5. Semilog plot of the directly obtained energy spectra from graphite (top) and those sample curves but divided by the number of counts $N(E)$, which increases counts proportionally to the SEE energy (bottom). Energy spectra for primary beam energies of 100, 200, 300, 400, and 500 eV are shown.

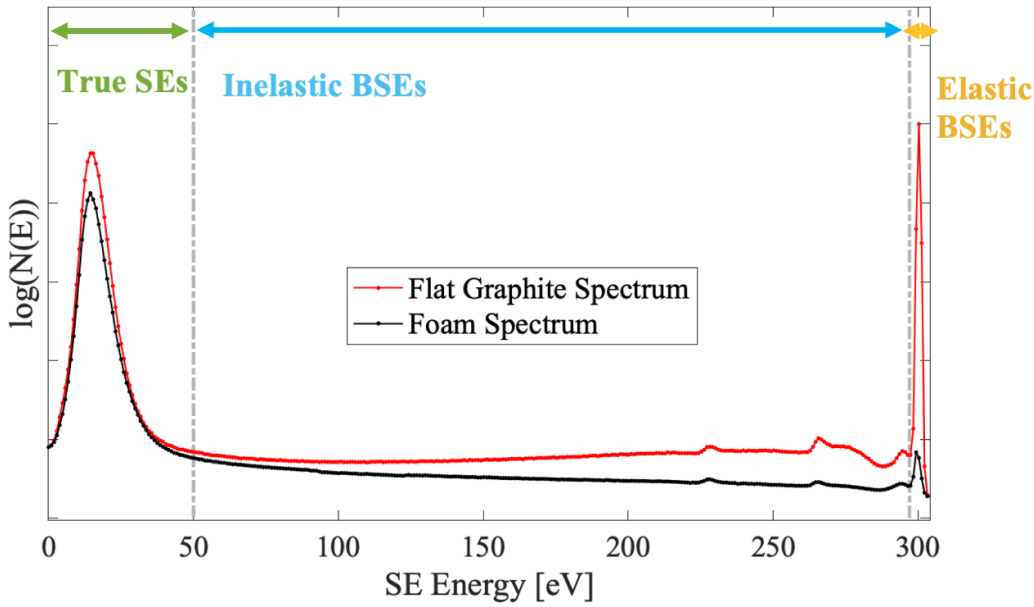

Figure 6. EEDF of flat graphite compared to 100 PPI foam for a primary electron beam energy of 300 eV. True SEs are between 0–50 eV, iBSEs between 50 eV and the primary energy (PE) minus 5 eV, and eBSEs are within the region of the PE $\pm$5 eV. Compared to the EEDF for flat graphite, the SE peak for the foam is reduced by 15% while the eBSE peak for the foam is reduced by 85% for this EEDF. There are zero counts at -10 eV and at PE plus 5 eV, but the data presented here is shifted above zero for clarity.

in figure 6 and can be described as:

$$N_{\mathrm{SE,\,true}} = \int_{0\,\mathrm{eV}}^{50\,\mathrm{eV}} N(E)\,\mathrm{d}E \tag{7}$$

$$N_{\mathrm{iBSE}} = \int_{50\,\mathrm{eV}}^{\mathrm{PE}-5\,\mathrm{eV}} N(E)\,\mathrm{d}E \tag{8}$$

$$N_{\mathrm{eBSE}} = \int_{\mathrm{PE}-5\,\mathrm{eV}}^{\mathrm{PE}+5\,\mathrm{eV}} N(E)\,\mathrm{d}E \tag{9}$$

and the total SEE signal (in arb. counts) is:

$$N_{\mathrm{SEE,\,tot}} = \int_{0\,\mathrm{eV}}^{\mathrm{PE}+5\,\mathrm{eV}} N(E)\,\mathrm{d}E. \tag{10}$$

The SEE yield can also be estimated by using the measured value of I_{PE} and a multiplication factor F found from the direct SEE measurements to convert electron counts to SEE current. F was determined experimentally from the flat graphite

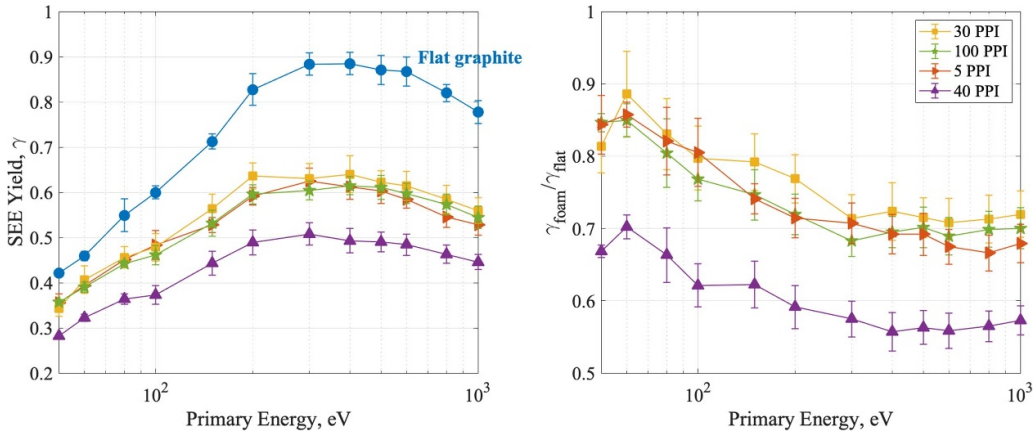

Figure 7. (left) Total SEE yield of flat graphite and four foams with different PPIs as a function of incident primary electron energy. Each data point is an average of five adjacent locations across the sample surface (right) reduction of yield compared to flat graphite for foam as a function of primary energy. The primary energy is set with <2 eV precision.

yield measurements in the direct SEE setup, γ_{tot}, found from equation (6). Total (integrated) counts N were on the order of $10^5 - 10^6$ counts/s, while the primary current I_{PE} was on the order of 100–500 nA. Thus, the factor F was determined using:

$$F = \frac{\gamma_{\text{tot}} I_{\text{PE}}}{N} \tag{11}$$

and was found to be $4.8 \pm 0.5 \times 10^{11}$ for all measured primary energies. Thus, the SEE yield determined from the CMA measurements can be inferred:

$$\gamma_{\text{tot, CMA}} = \frac{I_{\text{SEE}}}{I_{\text{PE}}} = \frac{F N_{\text{SEE}}}{I_{\text{PE}}}. \tag{12}$$

The relative contributions of SEE populations (true SEs, iBSEs, eBSEs) to the total SEE yield can then be found by using the CMA-derived electron energy spectra:

$$\text{true SE } \% = \frac{\gamma_{\text{SE, true}}}{\gamma_{\text{tot, CMA}}} \tag{13}$$

$$\text{iBSE } \% = \frac{\gamma_{\text{iBSE}}}{\gamma_{\text{tot, CMA}}} \tag{14}$$

$$\text{eBSE } \% = \frac{\gamma_{\text{eBSE}}}{\gamma_{\text{tot, CMA}}}. \tag{15}$$

This calculation is helpful to gain insight on the generation and suppression of SEs from the carbon foam compared with flat graphite and will be used in the following sections.

3. Results and discussion

3.1. Total SEE yield as a function of PE and reduction from flat graphite

Four carbon foam samples and flat graphite were measured for their SEE yield as a function of incident electron energy using the setup shown in figure 2, and results are shown in figure 7. The flat graphite has a maximum yield of $\gamma = 0.89$ at an incident PE of 300 eV, which is within 5% of previous measurements taken in the same setup [49]. The carbon foams followed a similar increasing SEE yield for 0–300 eV primary energies and decreasing SEE yield for >300 eV primary energies. The reduction of SEE yield compared to a flat is also shown in figure 7. It is important to note that the reported SEE suppression refers to the projected-area-normalized yield, relative to the same beam area on a flat material. The maximum reduction in SEE yield is achieved by the 40 PPI foam at all energies, with a $44 \pm 2\%$ yield reduction compared to flat graphite.

3.2. Angular dependence of SEE yield

To examine the effect of oblique primary electron incidence on SEE yield for foams with high anisotropy and no transparency to a backplate and low anisotropy with high backplate transparency, foams with 100 and 5 PPI were tilted on the sample stage using the setup shown in figure 2. Planar graphite is expected to increase in yield roughly as a function of $\sec\theta_{\text{i}}$ where θ_{i} is the angle of incidence [2]. By moving the x-linear stage, it was also possible to measure the 5 PPI foam with and without the graphite base, as shown in figure 2. The 5 PPI foam sample has a transparency of 20% and therefore it is important to measure the backplate contribution to the total SEE yield. Figure 8 shows results for the 5 PPI foam with and without a backplate, for 100 PPI foam, and for the backplate only (flat graphite).

The SEE yield for the 5 PPI foam without a backplate monotonically decreases for angles between $-15°$ and $15°$, but is roughly constant for angles between $15°$ and $35°$. The increased yield to the left of $15°$ could be at incident angles where the ligament side area is primarily exposed to the beam. As the foam is tilted, the yield may decrease as the beam becomes more aligned to the average ligament direction. This suggests that a low PPI foam is 'directional' in its geometry, similar to results found for fibrous surfaces [32, 42].

It is also apparent that a 5 PPI foam (20% transparency) with a backplate has a lower overall SEE yield than the same

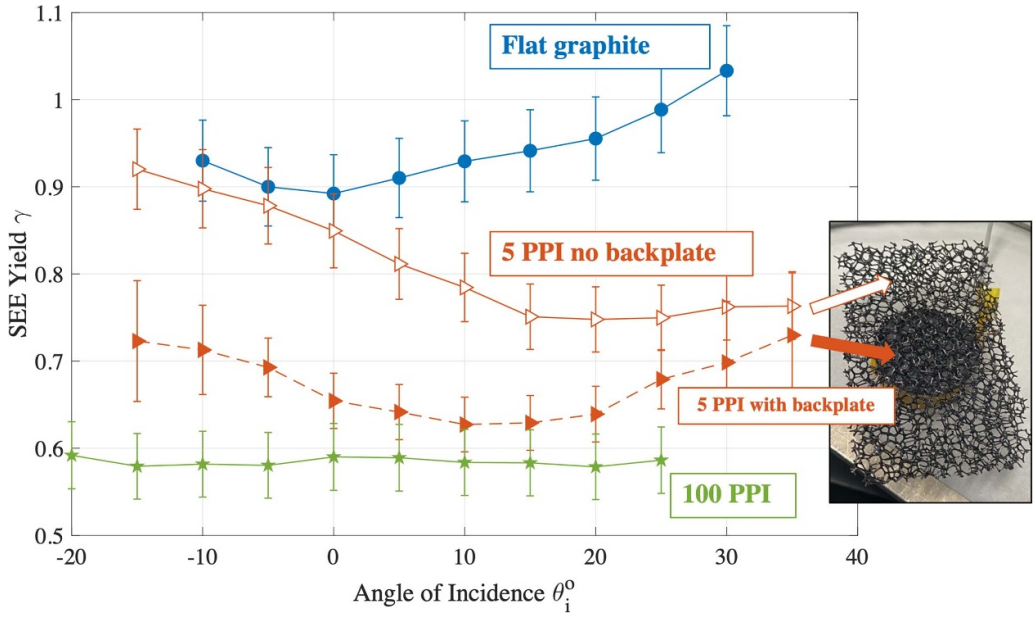

Figure 8. Total SEE yield as a function of the incident primary electron angle of incidence, θ_i. Measurements are shown for planar flat graphite, reticulated carbon foam with the largest pores (5 PPI) and 20% transparency with and without a backplate, and the foam with the smallest pores (100 PPI) with 0% transparency. The sample stage has a tilt accuracy of $\pm 1^\circ$.

PPI foam measured without a backplate. A possible explanation is as follows. SEE yield is due to successfully escaped electrons divided by the impeding electrons for every layer. The overall yield is the mean of the yield from each layer, weighted by the impeding electron flux. Each subsequent layer has a decreasing yield due to geometric trapping of the escaping secondaries. Therefore, for every added thickness of the foam layers, the overall yield decreases. This effect should be the same when adding a backplate.

The 5 PPI foam with a backplate appears to be symmetric around 10–15 degrees, which suggests the foam might have ligaments which are, on average, tilted by 10–15 degrees. When the foam is 'upright' at this angle, the backplate becomes most visible to the primary electron beam, which decreases the yield on average compared to when there is no backplate. While tilting the foam further, the transparency of the backplate to the primary beam decreases once more, and the yield increases.

Notably, results in figure 8 also show that the 100 PPI foam exhibits a loss of angular dependence with the primary electron beam. This result is similar to measurements taken of plasma-generated tungsten fuzz [14]. 100 PPI foam has ligament and pore dimensions between 10–80 μm, which is up to 100 times smaller than the electron beam diameter. It is possible that for such small features, the isotropic nature of the foams results in an average reduced SEE yield for each primary beam angle.

These results suggest that when the characteristic feature sizes of the foam are much smaller than both the beam diameter and the true SE escape depth (1–50 nm), the SEE is isotropic and the macroscopic secant dependence trend is averaged out. In the 100 PPI foam, the SEE is nearly angle-independent. In contrast, for a 5 PPI foam, the ligament orientation is resolved at the beam scale, and the exposed side-wall area varies with tilt. Therefore the effective emission area and escape cone change with the incident angle, resulting in the observed direction SEE yield response.

3.3. c. Comparison with analytical model for particle sputtering and electron emission (AMPS-E)

Each carbon foam was also analyzed for its SEE yield behavior as a function of PPI for a fixed PE of 300 eV. The results are shown in figure 9 along with comparisons with two analytical models, i.e. AMPS-E [58] and the Swanson and Kaganovich model [34]. This model was computed for a range of PPIs and two aspect ratios to simulate the foams measured in the direct measurement experiments. The shaded areas represents the error region. In addition, the direct SEE yield measurements were compared to SEM measurements recently reported [38]. Agreement was within 6% for AMPS-E and the direct measurements, and within 10% for the Swanson and Kaganovich models for foams with PPI > 5.

SEE yield is also shown in figure 9, and circled by a dotted black line, for a carbon foam with 40 PPI. In general, it may be expected that a foam with a backplate exhibits a minimum SEE yield for a fixed aspect ratio and varying PPI (or thickness, equivalently). At both zero and infinite PPI, the SEE yield should be close to that of planar carbon, and a minimum SEE yield may be achieved for the PPI at which the transparency reaches zero. Increasing PPI from zero decreases the yield as additional layers increase SE trapping until the open area seen by the incoming beam is zero. Then, the yield may increase again as additional ligament SE emission dominates the total SEE yield over trapping effects.

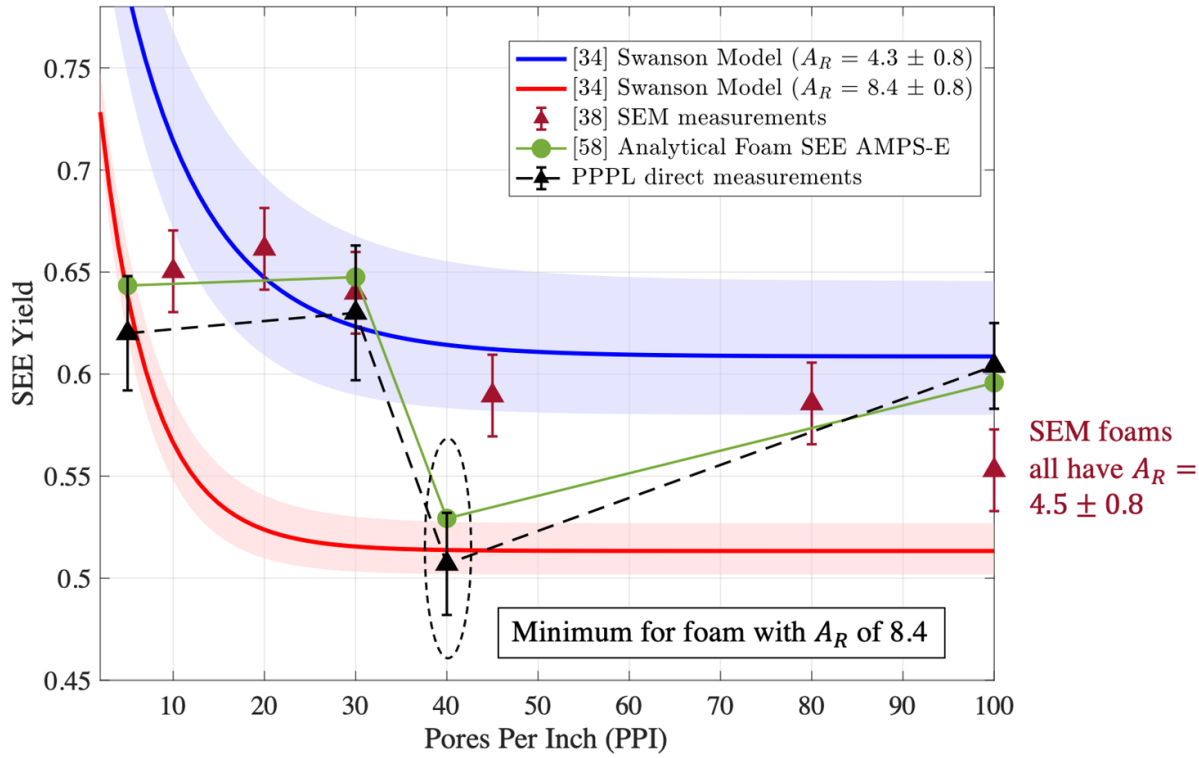

Figure 9. Direct measurements of four carbon foams are compared to two models [24, 34] and to previous SEM measurements [38]. A minimum SEE yield configuration is circled by the black dotted line and confirmed by these models. The 40 PPI foam and the model inputs have aspect ratio of $A_R = 8.4$, while the rest of the foams, including those that produced the SEM data points, have aspect ratios of $4.3 < A_R < 5.3$.

In this study, the lowest yield is likely due to the fact that the measured 40 PPI foam is the only foam with an aspect ratio $A_R = 8.4$, while all the other foams tested, including the SEM experiments [38], have aspect ratios between 4.3 and 5.1. At higher A_R, the pores are wider relative to the ligament thickness, allowing PEs and SEs to penetrate deeper into the foam. This increases the likelihood that emitted SEs are intersected by nearby ligaments thereby increasing trapping at intermediate PPI. By contrast, the 100 PPI foam combines negligible transparency with a much higher ligament density. These features increase the effective emission area and the likelihood of true SE generation on non-normal surfaces, which offsets trapping and raises the yield above the 40 PPI value. Thus, the observed trend reflects a physical balance between increased trapping at intermediate PPI and SE generation on dense, curved ligaments at very high PPI. For a foam with PPI = 5, the [58] model, which uses a view-factor analytical approach, agrees more closely than the Swanson and Kaganovich model [34], underlining the importance of using experimental data to validate and refine computational models for SEE from complex surfaces.

3.4. Reduction of low-energy SEs and BSEs

The SEE currents were found by integrating the indicated sections of curves shown in figure 6 and applying equations (7)–(15) to the measurements, and the total SEE current was found by integrating the entire CMA spectrum. The current reductions between flat graphite and 100 PPI foam for each SE population (true, eBSE and iBSE) are shown in figure 10. The true SE peak is reduced by ≈20% while the elastic backscattered peak is reduced by up to 70% when compared to that for a flat surface.

The relative contributions from the three SE populations to the total SEE yield was also calculated from the CMA data. The results in figure 11 show that the contribution of true SEs to the total SEE is larger for a foam than for a flat graphite sample. The percent contribution of SE energy populations found in the study reported herein is in agreement with measurements of planar graphite for 100 eV, 300 eV, and 500 eV primary electron energies [53]. Figure 11 results may imply that while the reticulated carbon foams are effective at trapping scattered, or specular electrons, the generation of low energy, true SEs may be enhanced.

Two possible mechanisms were explored to determine the cause of increased true SE contribution to total yield for the 100 PPI foam. One is to consider the generation of tertiary true SEs by redirected BSEs, and the second is an increased true SE production due to curved ligament surfaces where the primary electron beam strikes the foam at non-normal angles. Both hypotheses were examined using simple mathematical descriptions, the details of which are in appendix A.1. For the tertiary generation case, a correlation is developed between the true SE counts, $N_{\text{SE, true}}$, measured by the CMA and the expected SE counts based on geometric trapping of reflected eBSEs, $N_{\text{SE, expected}}$. $N_{\text{SE, expected}}$ can be found by multiplying the flat

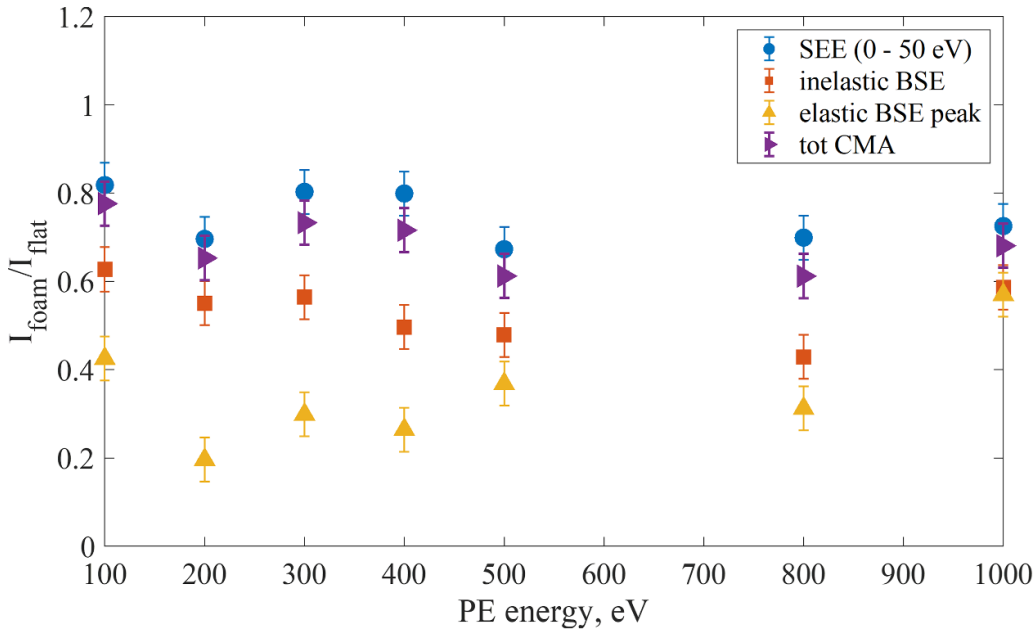

Figure 10. The reduction of SE, iBSe and eBSE yield from the 100 PPI foam sample was calculated using data collected with the CMA setup. Total SEE yield reduction agrees within 8% to direct measurement results. The SEE peak reduced by ≈20% but BSE was reduced by ≈60%–75% compared to the flat graphite.

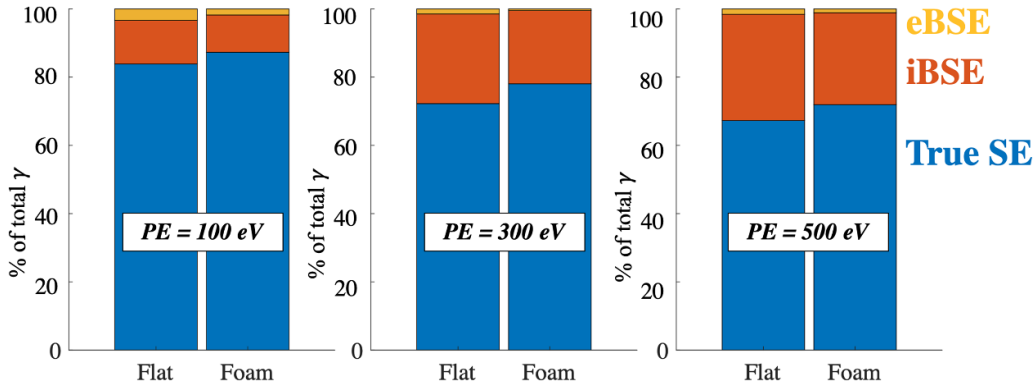

Figure 11. Relative % contribution of true SEs (blue), iBSE (red) and eBSE (yellow) to total SEE yield calculated for three different primary energies are shown. These results suggest SE is increased by 2%–5% from foam surfaces, while BSEs are suppressed. However, the contribution of iBSE and eBSE to the total yield is <40% at every energy.

graphite true SE counts by the reduction of foam to flat eBSE counts for each PE.

This reduction ratio is equivalent to the yellow markers in figure 10. The discrepancy between expected and measured true SEs from a foam are compared to the trapped total BSE fraction in the foam to infer if tertiaries generated from these BSEs can account for excess measured true SEs. For the angular consideration, the average increase in yield from a circular ligament of a foam compared to a flat surface was found to increase yield approximately by a factor of $\pi/2$. This factor was applied to the expected foam SE counts and compared to the measured SE counts. It was found that $N_{\mathrm{SE,\,true}}$ was 1.5 to 3 times larger than the measured value of $N_{\mathrm{SE,\,true}}$, and that accounting for BSE-generated tertiary and angular true SE contributions mitigates this discrepancy between 500–1000 eV PE, while at 100–400 eV these considerations were not sufficient to describe the additional true SE measured from a 100 PPI foam. A further qualitative and detailed investigation may be required to fully describe the mechanisms by which SE generation is enhanced, but an initial analysis has shown that high energy BSEs may generate lower energy SEs, and curved ligaments can also contribute to higher true SE populations.

4. Conclusions

In summary, this work has shown a reduction of SEE yield from a reticulated carbon foam surface with PPI ranging from 5 to 100 compared to planar graphite via a direct measurement method. The greatest reduction of $44 \pm 2\%$ is in agreement with recent results and analytical models, and a significant SEE reducing foam configuration with an aspect ratio

of 8.4 and 40 PPI was demonstrated. Previous studies using reticulated copper foams with larger volume fill fraction (4.6 % compared to the carbon foams of 3% [37]) examined foams of 100 PPI with a maximum reduction of 20%. The results presented in this work are consistent with the hypothesis that more reticulation (lower volume fill fraction) will increase the yield reduction.

By tilting the sample with respect to the primary incident electron beam, small pore, highly anisotropic foams of 100 PPI with no transparency of the primary electrons to a backplate displayed a 'fuzz-like' behavior with loss of angular dependence. Directional and non-uniform angular behavior was found for large pore foams of 5 PPI, much like previous results for the angular dependence of SEE yield from high aspect ratio carbon fibers.

Spectroscopic analysis of emitted SEs using a CMA was used to measure the SEE energy spectrum from a 100 PPI foam and a flat graphite sample. Results show that not all SE populations are suppressed equally: high energy elastic BSEs experience up to 80% suppression, while true SEs are reduced by up to only 68%. It was also found that a high PPI foam is more effective at trapping BSE electrons than true SEs. For both surfaces, the total low energy true SE electrons contribute more than 50% to the total yield. However, the relative contribution of each SE population differs between the two surface geometries: 100 PPI foam has true SE contribution that is 2%–3% more than that for the flat graphite. An initial analysis detailed in appendix A.1 and summarized in figure A1 shows that the increased true SE from foam surfaces could be due both to a tertiary population of true SEs generated from redirected BSE intersecting other ligament surfaces and due to curved ligament surfaces generating higher SEE yield by a factor of $\sec\theta_i$.

The findings presented in this work may have beneficial implications for applications when SEE yield is not desired, such as for plasma-facing components in fusion first walls, plasma propulsion components, RF components experiencing multipactor breakdowns, and spacecraft materials where ion-, photon-, and electron -induced SEE yield may cause anomalous charging and arcing. Insight into the mechanisms of low and high energy SEE suppression in foams can also be of importance to systems where electron emission enhancement is desired, such as emissive cathodes and electron microscopy, and informs the design space for optimizing the geometry of volumetrically complex materials for electron emission performance.

Data availability statement

All data that support the findings of this study are included within the article (and any supplementary files).

Acknowledgments

The authors thank Tim Bennett for technical assistance with the experiments. This work was supported by the Advanced Research Projects Agency–Energy (ARPA-E), U.S. Department of Energy, under Award No. DE-AR0001378 (AMPERE—Advanced Materials for Plasma-Exposed Robust Electrodes); and by the U.S. Department of Energy, Office of Fusion Energy Sciences, under Contract No. DE-AC02-09CH11466, as part of the Princeton Collaborative Low Temperature Plasma Research Facility (PCRF).

Author contributions

Angelica Ottaviano 0000-0003-0255-3824
Conceptualization (equal), Data curation (equal), Formal analysis (equal), Funding acquisition (equal), Investigation (equal), Methodology (equal), Writing – original draft (equal), Writing – review & editing (equal)

Gary Wan 0000-0003-3423-1440
Data curation (equal), Formal analysis (equal), Investigation (equal), Methodology (equal), Writing – review & editing (equal)

Yevgeny Raitses 0000-0002-9382-9963
Formal analysis (equal), Investigation (equal), Methodology (equal), Project administration (equal), Resources (equal), Supervision (equal), Visualization (equal), Writing – review & editing (equal)

Evan T Ostrowski 0000-0002-0261-2508
Data curation (equal), Validation (equal), Writing – review & editing (equal)

Shota Abe
Investigation (equal), Methodology (equal), Resources (equal), Software (equal), Writing – review & editing (equal)

Bruce E Koel 0000-0002-0032-4991
Investigation (equal), Methodology (equal), Supervision (equal), Writing – review & editing (equal)

Richard E Wirz
Conceptualization (equal), Funding acquisition (equal), Investigation (equal), Project administration (equal), Resources (equal), Supervision (equal), Validation (equal), Writing – review & editing (equal)

Appendix. Consideration of additional true SE generation from foams

A simple mathematical description is used to illustrate the process. Let X be defined as the geometric trapping (or SEE reduction factor) between a foam and a flat surface:

$$X = N_{\mathrm{eBSE,\ foam}}/N_{\mathrm{eBSE,\ flat}} \tag{A.1}$$

where $N_{\mathrm{eBSE,\ foam}}$ and $N_{\mathrm{eBSE,\ flat}}$ are respectively the foam and flat elastic BSE counts measured by the CMA. For simplicity, we assume the geometric trapping suppression factor, X, is best described by considering only specular reflected eBSEs.

The true SE count from the foam based on geometric trapping is therefore expected to be:

$$N_{\text{SE, expected}} = N_{\text{SE, flat}} \cdot X. \tag{A.2}$$

It was found that $N_{\text{SE, measured}} > N_{\text{SE, expected}}$ where $N_{\text{SE, measured}}$ is the SE count measured by the CMA defined in equation (7). This inequality suggests an additional SE generation mechanism.

A.1. Generation of tertiary true SEs from trapped BSEs in a foam

The additional SE expected, $N_{\text{SE, additional}}$ from a tertiary generation from BSEs can be estimated as:

$$N_{\text{SE, additional}} = N_{\text{BSE, flat}} \cdot \gamma_{\text{flat}} \cdot (1 - X) \tag{A.3}$$

where

$$N_{\text{BSE}} = N_{\text{eBSE}} + N_{\text{iBSE}}. \tag{A.4}$$

since it is assumed that both elastic and inelastic BSEs may generate tertiary electrons. γ_{flat} is a function of incident electron energy which varies from 0.7 to 0.9 for the energies considered. In these calculations, an average value of γ_{flat} was used.

Comparing the sum of the additional true foam SE and calculated foam SE, it is found that $N_{\text{SE, additional}} + N_{\text{SE, expected}} < N_{\text{SE, expected}}$. This suggests that tertiary SE generation from trapped BSEs alone is not sufficient to account for increased SE.

A.2. Generation of true SE from curved ligaments

Additional true SEs can be generated from the curved surface of a foam ligament compared to flat graphite. To estimate the additional contribution of curved ligament surfaces, the ligaments are approximated as half-circles. True SE yield increases as approximately $\sec\theta_i$, and averaging the increased yield over a half circle gives:

$$\int_0^{\pi/2} \gamma_{\text{flat}} \sec\theta \cos\theta \, \mathrm{d}\theta = \frac{\gamma_{\text{flat}}\pi}{2}. \tag{A.5}$$

Thus, compared to flat graphite, the foam true SE yield should be larger by a factor of 1.57. Figure A1 shows the expected SE from foam based only on geometric trapping (blue), and the measured actual foam SE (red), as well as additional contributions from tertiary SEs and angular-based increase by a factor of 1.57. Figure A1 also shows the measured SE counts from the CMA ($N_{\text{SE, measured}}$) for a foam with 100 PPI, the expected value from only geometric trapping, the expected value plus tertiary SE generation, and the expected value plus tertiary and non-perpendicular angular contributions from the curved ligament surfaces.

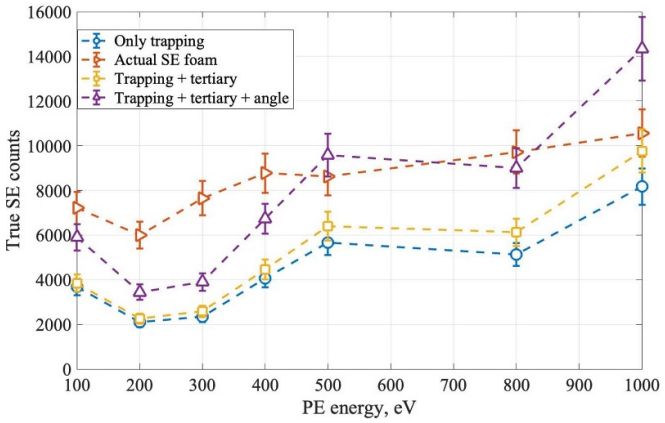

Figure A1. True SE counts measured (red) and calculated based on geometric trapping alone (blue), a tertiary true SE contribution (yellow) and a tertiary and angular contribution (purple).

References

[1] Scholtz J, Dijkkamp D and Schmitz R 1996 *Philips J. Res.* **50** 375–89
[2] Bruining H 2016 *Physics and Applications of Secondary Electron Emission: Pergamon Science Series: Electronics and Waves—a Series of Monographs* (Elsevier)
[3] Hobbs G and Wesson J 1967 *Plasma Phys.* **9** 85
[4] Raitses Y, Kaganovich I D, Khrabrov A, Sydorenko D, Fisch N J and Smolyakov A 2011 *IEEE Trans. Plasma Sci.* **39** 995–1006
[5] Graves T, Spektor R, Stout P and Axley A 2009 *Phys. Plasmas* **16** 083502
[6] Vaughan J R M 1989 *IEEE Trans. Electron Devices* **36** 1963–7
[7] Goebel D M, Katz I and Mikellides I G 2023 *Fundamentals of Electric Propulsion* (Wiley)
[8] Katz I, Mandell M, Jongeward G and Gussenhoven M 1986 *J Geophys. Res.: Space Phys.* **91** 13739–44
[9] Lai S T 2013 *IEEE Trans. Plasma Sci.* **41** 3492–7
[10] Balcon N, Payan D, Belhaj M, Tondu T and Inguimbert V 2011 *IEEE Trans. Plasma Sci.* **40** 282–90
[11] Kirby R E and King F 2001 *Nucl. Instrum. Methods Phys. Res. A* **469** 1–12
[12] Yin Vallgren C 2011 Low secondary electron yield carbon coatings for electron cloud mitigation in modern particle accelerators *CERN-THESIS-2011-063 (CERN)*
[13] Capece A, Patino M, Raitses Y and Koel B 2016 *Appl. Phys. Lett.* **109** 011604
[14] Patino M, Raitses Y and Wirz R 2016 *Appl. Phys. Lett.* **109** 201602
[15] Langendorf S and Walker M 2015 *Phys. Plasmas* **22** 033515
[16] Taccogna F, Longo S and Capitelli M 2004 *Phys. Plasmas* **11** 1220–8
[17] Sydorenko D, Smolyakov A, Kaganovich I and Raitses Y 2006 *IEEE Trans. Plasma Sci.* **34** 815–24
[18] Bonaventura Z, Bílek P, Tungli J and Šimek M 2022 *Plasma Sources Sci. Technol.* **31** 035003
[19] Lee J H *et al* 2021 *J. Geophys. Res.: Space Phys.* **126** e2020JA028650
[20] Diaz-Aguado M F, Bonnell J W, Bale S D, Christensen J, Lundgreen P, Lee J, Dennison J, Wood B and Gruntman M 2020 *J. Spacecr. Rockets* **57** 793–808
[21] Vincie M J 2019 Wright-Patterson air force base
[22] Miyake H, Nitta K, Michizono S and Saito Y 2007 *Shinku* **50** 378–81
[23] Lee J *et al* 2024 Miniaturized plasma sensors *AGU Fall Meeting Abstracts* vol 2024 p SA01–29

[24] Ottaviano A, Li G, Huerta C, Thuppul A and Chen Z Dodson C and Wirz R 2019 Plasma-material interactions for electric propulsion: challenges *Approaches and Future The 36th Int. Electric Propulsion Conf., (Austria)*
[25] Burdovitsin V, Zolotukhin D, Oks E and Panchenko N 2019 *J. Phys. D: Appl. Phys.* **52** 285204
[26] Van Oost G 2016 Advanced probe edge diagnostics for fusion devices *J. Phys.: Conf. Ser.* vol 666
[27] Knoll G F 2010 *Radiation Detection and Measurement* (Wiley)
[28] Shih A, Yater J, Hor C and Abrams R 2002 *IEEE Trans. Electron Devices* **41** 2448–54
[29] Tao S X, Chan H W and Van der Graaf H 2016 *Materials* **9** 1017
[30] Simon R and Williams B 2007 *IEEE Trans. Nucl. Sci.* **15** 167–70
[31] Chopra N S 2025 Boundary-induced kinetic effects in low temperature E×B plasmas *PhD Thesis* Princeton University
[32] Swanson C and Kaganovich I D 2016 *J. Appl. Phys.* **120** 213302
[33] Ye M, He Y, Hu S, Wang R, Hu T, Yang J and Cui W 2013 *J. Appl. Phys.* **113** 074904
[34] Swanson C and Kaganovich I D 2018 *J. Appl. Phys.* **123** 023302
[35] Alvarado A, Chang H-Y, Nadvornick W, Ghoniem N and Marian J 2019 *Appl. Surf. Sci.* **478** 142–9
[36] Li G Z and Wirz R E 2021 *Phys. Rev. Lett.* **126** 035001
[37] Dickstein D, Chang H-Y, Marian J, Feldman M, Hubble A, Spektor R and Ghoniem N 2020 *J. Appl. Phys.* **128** 123302
[38] Ottaviano A and Wirz R E 2023 *J. Appl. Phys.* **133** 103302
[39] Sabiston G and Wirz R E 2024 *J. Appl. Phys.* **135** 183301
[40] Gao E, Nadvornick W, Doerner R and Ghoniem N M 2018 *J. Nucl. Mater.* **501** 319–28
[41] Amatriain A, Gargiulo C and Rubio G 2023 *Int. J. Heat Mass Trans.* **217** 124701
[42] Ottaviano A, Banerjee S and Raitses Y 2019 *J. Appl. Phys.* **126** 223301
[43] Huerta C E and Wirz R E 2016 Surface geometry effects on secondary electron emission via Monte Carlo modeling *52nd AIAA/SAE/ASEE Joint Propulsion Conf.* p 4840
[44] Goldstein J I, Newbury D E, Michael J R, Ritchie N W, Scott J H J and Joy D C 2017 *Scanning Electron Microscopy and x-ray Microanalysis* (springer)
[45] Cazaux J 2012 *J. Electron Microsc.* **61** 261–84
[46] Koshikawa T and Shimizu R 1974 *J. Phys. D: Appl. Phys.* **7** 1303
[47] Knapp J, Lapeyre G, Smith N and Traum M 1982 *Rev. Sci. Instrum.* **53** 781–4
[48] Modinos A 1984 Secondary electron emission spectroscopy *Field, Thermionic and Secondary Electron Emission Spectroscopy* (Springer) pp 327–45
[49] Jin C, Ottaviano A and Raitses Y 2017 *J. Appl. Phys.* **122** 173301
[50] Dunaevsky A, Raitses Y and Fisch N 2003 *Phys. Plasmas* **10** 2574–7
[51] Raitses Y, Kaganovich I and Sumant A 2013 Electron emission from nano-and micro-engineered materials relevant to electric propulsion *Proc. 33rd Int. Electric Propulsion Conf.* (USA)
[52] Capece A M and Enriquez A 2024 *J. Appl. Phys.* **58** 035206
[53] Patino M, Raitses Y, Koel B E and Wirz R 2015 *J. Phys. D: Appl. Phys.* **48** 195204
[54] Chase R, Gordon W and Hoffman R 1980 *Appl. Surf. Sci.* **4** 271–81
[55] Schmierer E N and Razani A 2006 1194–203
[56] Ottaviano A 2023 *Plasma Interactions and Electron Dynamics for Volumetrically Complex Materials* (University of California)
[57] Nishchak O Y, Savchenko N, Streletsky O, Zykova E Y and Khvostov V 2019 Electron spectroscopy of various nanostructured carbon films *J. Phys.: Conf. Ser.* **1238** 012034
[58] Ottaviano A and Wirz R 2022 *Int. Electric Propulsion Conf.* vol 595